APPLIED SCIENCES AND ENGINEERING

Ultrafast rotation of magnetically levitated macroscopic steel spheres

Marcel Schuck,[1]* Daniel Steinert,[2] Thomas Nussbaumer,[2] Johann W. Kolar[1]

Our world is increasingly powered by electricity, which is largely converted to or from mechanical energy using electric motors. Several applications have driven the miniaturization of these machines, resulting in high rotational speeds. Although speeds of several hundred thousand revolutions per minute have been used industrially, we report the realization of an electrical motor reaching 40 million rpm to explore the underlying physical boundaries. Millimeter-scale steel spheres, which are levitated and accelerated by magnetic fields inside a vacuum, are used as a rotor. Circumferential speeds exceeding 1000 m/s and centrifugal accelerations of more than 4×10^8 times gravity were reached. The results open up new research possibilities, such as the testing of materials under extreme centrifugal load, and provide insights into the development of future electric drive systems.

INTRODUCTION

Electric motors and generators have seen widespread use in numerous applications since their invention. Fueled by applications such as centrifuges, drive systems for turbo compressors, machining spindles, flywheels, and generators for micro gas turbines, a trend toward miniaturization and increased power density of these machines has developed in recent years (*1*). The output power of a rotating machine is given by $P = \omega_m T$, with T and ω_m denoting its torque and angular frequency of rotation, respectively. Because the dimensions of a machine are mainly determined by its torque (*2*), this trend is facilitated by motors featuring low torque and high rotational speeds, which has sparked interest in the underlying physical limits. Some applications, for example, rotating mirror optical systems, directly demand for high rotational speeds (*3*), which have been explored industrially up to several hundred thousand revolutions per minute, and laboratory prototypes of microelectromechanical systems reaching 1.2 million rpm (Mrpm) have been demonstrated (*4*).

To reduce the bearing friction losses associated with high rotational speeds, magnetic suspension, in which the rotor is levitated without mechanical contact, can be applied. This system was initially proposed by Holmes (*5*) and used to produce high centrifugal fields by accelerating the levitated rotor. The highest measured rotational speed during these experiments of 37.98 Mrpm (rotational frequency of 633 kHz) was published in 1954 (*6*) with a rotating steel sphere of 0.521 mm in diameter, shortly before it was destroyed due to centrifugal forces. These high rotational speeds could not be reproduced in closely related experiments for more than six decades, despite significant advancements, especially in the field of control electronics. In the study of Katano and Shimizu (*7*), the smallest levitated rotor had a diameter of 1.5 mm and reached a rotational speed of 12.66 Mrpm (211 kHz). The usage of smaller rotors was limited by their electrostatic attraction to the surface of a glass vacuum chamber. More recently, a rotational speed of 2.88 Mrpm (48 kHz) was reached with a 1-mm sphere (*8*), which was limited by gas friction under medium vacuum conditions.

Experiments using circularly polarized light to accelerate microscale rotors have demonstrated rotational speeds of 330 Mrpm (5.5 MHz) by using an electrically trapped graphene flake of 0.4 μm in size (*9*). A rotational speed of 600 Mrpm (10 MHz) was demonstrated by Arita *et al.* (*10*) by using optically levitated birefringent crystals with a mean diameter of 4.40 μm. In the study of Lehmuskero *et al.* (*11*), spherical gold nanoparticles with an average radius of 200 nm were trapped in water against a glass surface and accelerated to approximately 180,000 rpm (3 kHz) by a polarized laser beam. The achievable rotational speed was limited by the occurring drag torques and substantial heating of the particle due to absorption of the laser power. Motors using rods in the micro- or nanoscale as rotors driven by various techniques are currently being researched but have been confined to comparatively low rotational speeds (*12*–*14*). The highest achieved rotational speed of this motor to date is 2.5 Mrpm (42 kHz) and it was reached with a gold nanorod driven by resonant light scattering (*15*). It was limited by the same factors as reported by Lehmuskero *et al.* (*11*) because of the similarities of the used techniques.

Here, we report the realization of an electric motor reaching a rotational speed of 40 Mrpm (667 kHz). To the authors' knowledge, this is the highest measured rotational speed for an electrically driven rotor. The developed system is aimed at exploring the physical boundaries and providing insights into future drive systems. Macroscopic solid steel spheres, as commonly used in ball bearings, with diameters down to 0.5 mm are used as rotors and levitated without mechanical contact by a magnetic suspension technique in vacuum. The drive torque is generated by the operational principle of a solid rotor induction machine. Compared to earlier works using similar principles (*6*, *7*), active stabilization of the rotor in all translatory degrees of freedom is used in this study. This allows the achievement of ultrahigh rotational speeds at high repeatability and facilitates quantitative studies using a variety of rotor samples. Because of the significantly larger rotor radii a, the centrifugal accelerations $a_r = \omega_m^2 a$ obtained in this study are of the same magnitude as the ones from Arita *et al.* (*10*) and above those reached by Kane (*9*). The occurring relative drag torques and losses are much lower than those in the studies of Lehmuskero *et al.* (*11*) and Shao *et al.* (*15*), thus significantly reducing rotor heating and the required drive torque for reaching ultrahigh rotational speeds.

RESULTS

An experimental setup was realized, which allows the acceleration of millimeter-scale spherical steel rotors to the desired rotational speeds. To prevent excessive drag due to gas and bearing friction, a magnetic suspension technique is applied and the rotor is spun in vacuum at

[1]Power Electronic Systems Laboratory, Swiss Federal Institute of Technology, Technoparkstrasse 1, 8005 Zurich, Switzerland. [2]Levitronix GmbH, Technoparkstrasse 1, 8005 Zurich, Switzerland.
*Corresponding author. Email: schuck@lem.ee.ethz.ch

pressures p under which free molecular flow conditions [Knudsen number (Kn) >> 1] apply. The setup is shown in Fig. 1.

Magnetic suspension

Levitation of the rotor without mechanical contact is achieved by counteracting the gravitational force by the magnetic reluctance force. This force exerted on the ferromagnetic rotor by the electromagnet is given as

$$\mathbf{F} = \frac{4}{3}\pi a^3 M_z \frac{\partial B_z(z_0)}{\partial z}\mathbf{e}_z \quad (1)$$

where M_z and $B_z(z_0)$ denote the magnetic moment of the rotor and the magnitude of the magnetic induction in the z direction at the levitation height z_0, respectively (*16*). The rotor position is continuously measured by optical position sensors, and a constant levitation height is maintained by closed-loop control of the electric current through the coil of the electromagnet. Because of the concentrated magnetic flux, the rotor is passively stable in the center of the setup in horizontal direction. Its horizontal dynamics with position $r(t)$ can be described as a pendulum by

$$m\ddot{r}(t) + b_r\dot{r}(t) + k_r r(t) = F_d \quad (2)$$

with rotor mass m, passive radial stiffness k_r generated by the centering core, and damping constant b_r. The rotor mass is in the range of 500 μg for steel spheres with 0.5 mm in diameter. For ambient pressure conditions, the damping coefficient due to laminar gas friction is obtained as $b_c = 6\pi\eta a$ to be in the order of 10^{-7} Ns/m, where η denotes

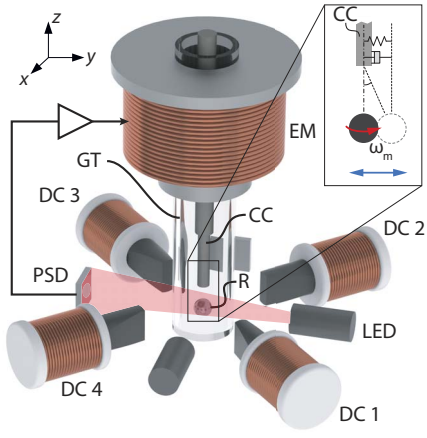

Fig. 1. High-speed magnetically levitated spinning ball motor. Experimental setup composed of a solid steel sphere rotor (R), which is levitated by means of an electromagnet (EM). The position of the rotor is measured in all dimensions with two orthogonally placed position-sensitive device (PSD) sensors onto which the shadow of the sphere is projected. Light is projected onto the rotor by two infrared light-emitting diodes (LEDs). The output signal is used for the closed-loop control of the levitation height. A centering core (CC) guides the magnetic flux toward the rotor. Four drive coils (DC 1 to 4) produce a rotating magnetic field, which exerts a torque on the rotor. To reduce drag due to air friction, the rotor is enclosed in a glass tube (GT), which is evacuated by a vacuum system. The inset shows a magnification of the rotor and the lower end of the centering core. Aside from spinning around the z axis as desired, the rotor is prone to oscillate horizontally, requiring active damping through closed-loop control. This behavior can be modeled as a weakly damped spring-mass pendulum.

the dynamic viscosity of the surrounding gas (air) (*17*). Under free molecular flow conditions, it is reduced to

$$b_{fm} = \left(\frac{4}{3} + \frac{\pi}{6}\right)\pi\rho a^2\bar{c} \quad (3)$$

in the order of 10^{-9} Ns/m (*18*). Here, ρ denotes the density of the gas and $\bar{c} = \sqrt{8k_B T_g/(\pi m_g)}$ is its mean thermal velocity with Boltzmann constant k_B, absolute gas temperature T_g, and mass of the gas molecules m_g. Because of this low horizontal damping, additional external damping needs to be used. In the studies of Beams (*6*) and Katano and Shimizu (*7*), this was achieved by a ferromagnetic damping needle, with its lower end floating in a viscous fluid below the rotor. Because the rotor and the needle are both magnetized by the electromagnet, the needle follows horizontal oscillations of the rotor due to magnetic coupling. Energy of the oscillation is dissipated by fluid drag at the lower end of the needle. Although this arrangement works well for rotors larger than ~1 mm, it was found to be unreliable for the desired smaller rotor sizes, which is in accordance with the findings of Beams (*19*). Instead, an active magnetic damping force F_d in horizontal direction is exerted on the rotor by the same principle as outlined in Eq. 1. This is achieved by closed-loop control of the currents in the horizontally arranged coils. By this technique, the rotor is levitated and stabilized in all directions. A photograph of the levitated rotor and the setup is shown in fig. S1.

Motor torque and drag

A motor torque for acceleration of the conductive rotor is generated by placing it into a rotating magnetic field, which is generated by the horizontally arranged coils. Consequently, in each of these coils, the flowing current consists of a superposition of the current necessary for stabilization of the rotor and that required for torque generation. Rotation of the magnetic field **B** for driving the rotor is obtained by phase-shifting the alternating drive currents in coils 1 to 4 by an angle of 0°, 90°, 180°, and 270°, respectively. Because of the difference of the mechanical angular rotational frequency of the rotor ω_m and the frequency ω_f by which the magnetic field rotates in the horizontal plane, eddy currents of density **J** are induced inside the rotor. The distribution of these eddy currents depends on the slip frequency $\omega_s = \omega_f - \omega_m$ and has been modeled by solving the underlying electromagnetic field problem (*20*). The motor torque originates from the interaction of the eddy currents with the external magnetic field and is obtained as

$$\mathbf{T}_m = \int_0^{2\pi}\int_0^{\pi}\int_0^{a}\mathbf{r}\times(\mathbf{J}\times\mathbf{B})r^2\sin\theta dr d\theta d\varphi \quad (4)$$

with r, θ, and φ denoting spherical coordinates.

This torque is counteracted by a drag torque due to gas friction. For ambient pressure and laminar flow conditions, this torque is obtained as $T_{lam} = 8\pi\eta a^3\omega_m$. Because of the small rotor radii, the occurring Reynolds numbers are limited to values below 2×10^4, suggesting that a laminar boundary layer around the sphere exists at all rotational speeds. The resulting drag torques can be obtained as $T_{bl} = 3.27\sqrt{\rho\eta}a^4\omega^{3/2}$, which is in the range of 10^{-7} Nm for a 0.5-mm sphere rotating at 40 Mrpm (*21*). Under free molecular flow conditions, the drag torque is reduced to

$$T_{fm} = 2/3\sigma_t\pi\rho\bar{c}a^4\omega_m \quad (5)$$

where the tangential momentum accommodation coefficient σ_t is approximately one for the technically smooth surfaces of the used steel balls (*22*). Evaluation yields a drag torque in the range of 10^{-14} to 10^{-9} Nm for vacuum pressures p of 10^{-4} to 1 Pa, respectively. This illustrates that operation under vacuum conditions is preferable because it reduces the required drive torque and, thereby, the occurring losses inside the rotor (see the next section for details). The modeled and measured torque characteristics of the motor including drag due to air friction are shown in Fig. 2A. The torque increases with the angular slip frequency due to a higher eddy current density inside the rotor. The overall torque acting on the rotor was obtained from an acceleration experiment as $T = I\dot{\omega}_m$, with $I = 8/15\pi\rho_r a^5$ being the moment of inertia of the rotor with material mass density ρ_r. Details regarding the procedure and uncertainty evaluation can be found in Materials and Methods. The residual between the measured and the modeled torque, as shown in the inset of Fig. 2A, is <15% for all slip frequencies and <5% for $f_s = \omega_s/(2\pi) > 250$ kHz. The increased deviation at low slip frequencies (high rotational speeds) is attributed to the low relative level of the motor torque, which increases the effect of the drag torque caused by the active magnetic damping in horizontal direction. Figure 2A (a and b) shows calculated exemplary eddy current density distributions $\mathbf{J}(r,\varphi)$ inside the rotor for two different values of f_s. They describe current loops inside the rotor for which the direction of the current flow is marked. The magnitude of the induced eddy currents is highest at the surface of the sphere due to the skin effect. The distributions differ as the amplification of the rotating external magnetic drive field inside the ferromagnetic rotor depends on the relative speed between the spatial rate of change of the drive field direction and the mechanical rotation of the sphere, which, in turn, affects the density of the eddy currents driven by this field inside the conductive rotor.

Additional drag torques of a similar magnitude to that of the air friction at pressures of 10^{-4} Pa are caused by eddy currents in the rotor due to directional changes and asymmetries in the magnetic suspension field (*23*). Nevertheless, the overall drag torque is at a low absolute level, allowing an undriven rotor to spin for multiple days at rotational speeds of several tens of million revolutions per minute.

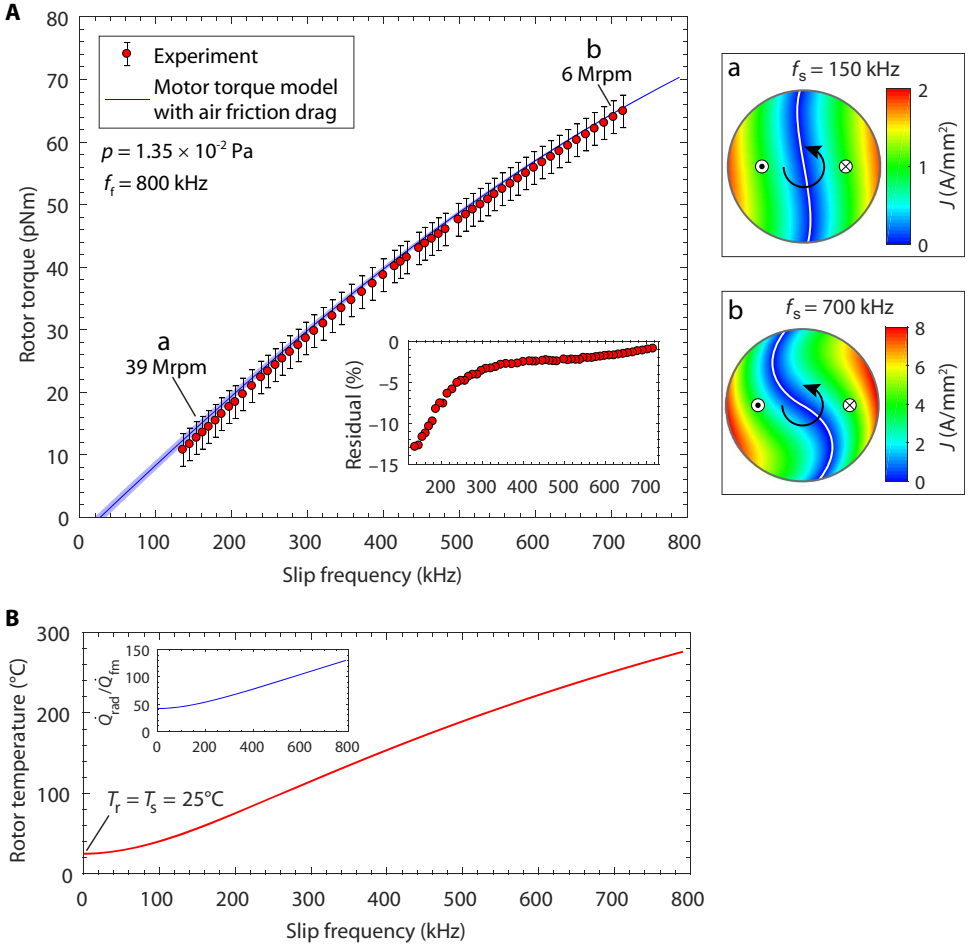

Fig. 2. Torque characteristics of the motor including air friction drag and temperature for a 0.5-mm rotor. (**A**) Torque acting on the rotor depending on the slip frequency for a field frequency of 800 kHz (synchronous rotational speed of 48 Mrpm). The shown error bars result from the calculation of the angular acceleration based on rotational speed measurements, which have a resolution of 500 Hz. The shaded blue area represents a ±30% uncertainty related to pressure measurement. The inset shows the residual between the experimentally obtained and the modeled torque using the read pressure value (blue line). Subfigures (a) and (b) show the current density distributions inside the rotor on the horizontal plane through its equator at slip frequencies of 150 and 700 kHz, respectively. (**B**) Rotor temperature over the same slip frequency range. The inset shows the ratio of heat transfer between the rotor and the environment due to radiation and free molecular conduction.

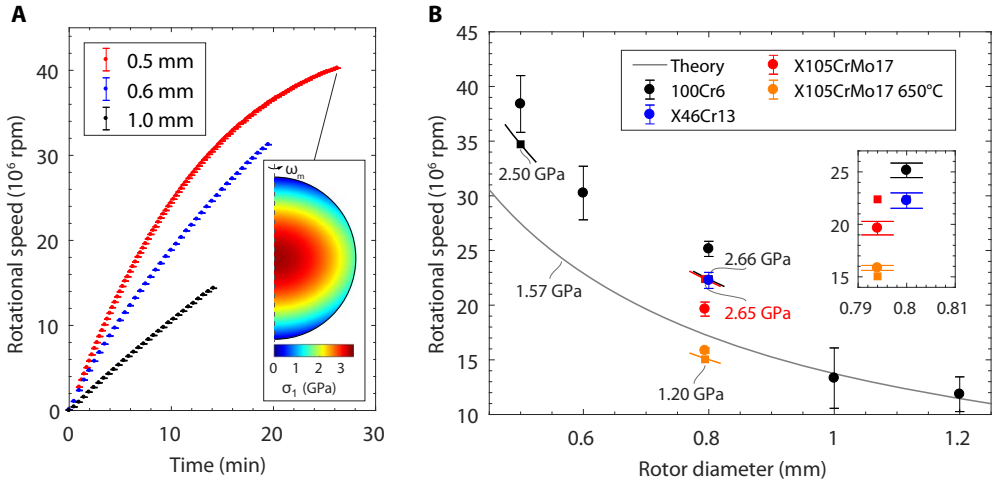

Fig. 3. Acceleration curves and bursting speeds of different rotors. (**A**) Acceleration curves for rotors of different diameters to their bursting speeds. Shown error bars represent the 500-Hz resolution of the measurements. The inset shows the highest of the principal normal mechanical stresses inside the rotor. (**B**) Achievable rotational speeds for different rotor sizes, materials, and initial stress conditions. Error bars show 95% confidence intervals for the mean. The inset shows a magnification of values for diameters 0.794 and 0.8 mm, illustrating the influence of the material and thermal treatment on the achievable rotational speed. The theoretical curve is based on the tabulated tensile strength value for 100Cr6 material. Short lines with square markers of the respective color correspond to calculated rotational speeds based on the specified UTS values obtained from hardness measurements (see text for details).

Rotor losses and heating

Heating of the rotor is caused by the eddy currents because of its finite conductivity σ. The overall power loss P_{ec} inside the rotor is obtained by integration of the loss density $p_{ec} = \mathbf{J}^2/\sigma$ over its volume, similar to Eq. 4. Heating should be limited such that the rotor temperature remains below ~150°C at high rotational speeds. Above this temperature, the ultimate tensile strength (UTS) of the used steels decreases (*24*), which limits the achievable rotational speed. Energy is transferred between the freely suspended rotor in vacuum and its surrounding by free molecular conduction and radiation.

The rate of energy transfer by radiation for the fully enclosed rotor inside the vacuum tube is $\dot{Q}_{rad} = 4\pi a^2 \sigma_B \varepsilon (T_r^4 - T_s^4)$, where σ_B, ε, T_r, and T_s denote the Stefan-Boltzmann constant, emissivity of the rotor (~0.1 for polished steel), its temperature, and the temperature of the surrounding, respectively (*25*). Emissivity characteristics of the surrounding surfaces can be neglected because their surface area is much larger than that of the considered small rotors.

The rate of free molecular heat transfer is

$$\dot{Q}_{fm} = \pi a^2 \alpha \frac{\bar{p}\bar{c}}{2} \frac{\gamma + 1}{\gamma - 1} \left(\frac{T_r}{T_s} - 1 \right) \quad (6)$$

where γ denotes the specific heat ratio of the surrounding gas, for which the temperature has been assumed to be T_s (*26*). The thermal accommodation coefficient α is a measure for the actual energy carried away by gas molecules leaving the rotor surface. Values of α = 0.87 to 0.95 are found in the literature for polished metal surfaces and air as a gas (*27*).

The resulting rotor temperature is obtained from the power balance $P_{ec} = \dot{Q}_{fm} + \dot{Q}_{rad}$ and is shown in Fig. 2B for the same experimental conditions under which the torque was acquired. It is limited to uncritical values at high rotational speeds and approaches T_s for low slip frequencies due to lower eddy current losses. The temperature increase of the rotor over the entire operating range is sufficiently low not to alter its material properties. The inset of Fig. 2B shows that heat transfer between the rotor and the surrounding due to radiation is roughly 40 to 130 times higher than that due to free molecular conduction. Consequently, the rotor temperature remains in the same range even for very low vacuum pressures.

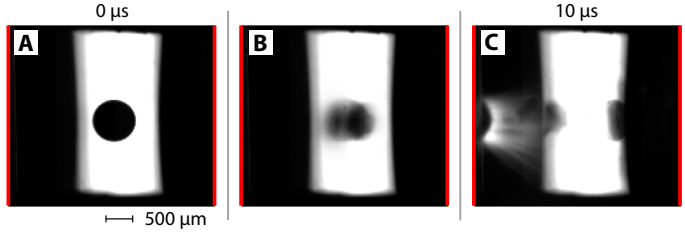

Fig. 4. Rotors exploding due to high centrifugal force. High-speed image sequence showing a rotor (*a* = 0.4 mm), initially intact one frame before exploding (**A**), fractured into multiple parts (**B**), and individual fractures hitting the wall of the vacuum tube (**C**). Red bars mark the walls of the vacuum tube. Images were recorded at 100,000 frames per second (fps) and a shutter speed of 1/283,000 s. The sequence is assembled by combining images from two different rotor explosions at 21.3 Mrpm (A and C) and 23.4 Mrpm (B) to enhance time resolution.

Achieved rotational speeds

Three exemplary acceleration curves to the bursting speeds of different rotors are shown in Fig. 3A. The rate of acceleration is decreased at higher rotational speeds because of a lower slip frequency. It is visible that smaller rotors are accelerated faster, as $I \propto a^5$, whereas $T_m \propto a^3$.

The achievable rotational speed is only limited by the mechanical stress because of centrifugal forces that the rotor material can withstand. An exemplary stress distribution is shown in the inset of Fig. 3A for steel with ρ_r = 7610 kg/m^3 and a Poisson's ratio ν = 0.3. Its maximum value occurs in the center of the rotor and is obtained as $\sigma_{1,max} = K \rho_r \omega_m^2 a^2$, where *K* is a shape- and material-dependent constant (*K* ~ 0.398 for the given case) (*28*). The achievable rotational speed is determined by the

UTS to density ratio of the rotor material as $\omega_{m,max} \propto 1/a\sqrt{\sigma_m/\rho_r}$, corresponding to a constant achievable circumferential speed $v_{c,max}$.

High variability was observed for the bursting speeds (Fig. 3B), which is attributed to fluctuations in the thermal treatment, initial stress conditions, and potential flaws of the rotor material. Anisotropies of residual stresses cause a dependency of the achievable rotational speed on the axis of rotation. An initial theoretical estimate of the achievable rotational speed was obtained by allowing a maximum normal stress (Rankine's theory) in the rotor center of 1570 N/mm^2, a value commonly found in the literature for the UTS of small size ball bearing spheres made from 100Cr6 material (*24*, *29*, *30*). The obtained values are in good agreement with those obtained experimentally for the bigger spheres tested in this study but underestimate the mean of the achievable rotational speeds for smaller spheres by up to 46%. In the study of Beams (*31*), this was attributed to a decreasing the probability of flaws in the rotor. An improved estimate for the achievable rotational speed was obtained by measuring the hardness of rotors with the same size and from the same manufacturing batch as those used in the acceleration experiments. The UTS values obtained from these measurements based on the model provided by Pavlina and Van Tyne (*32*) were found to be higher than the aforementioned value. The resulting calculated attainable rotational speeds are shown in Fig. 3B as lines with square markers alongside the respective UTS values. The deviation from the mean value of those reached in experiments is reduced to less than 12%. Further experiments were carried out with rotors that were thermally treated before acceleration to reduce and equalize the initial stressing. The hardness, UTS, and bursting speeds of these samples were significantly decreased. The variability of the attained rotational speeds was greatly reduced, with the range of all measured values lying within 2% of their mean. Predicted rotational speeds are within ~5% of the measured values for these samples, which is a significant improvement over the studies of Katano and Shimizu (*7*) and Beams (*31*). The remaining underestimation of the actually achievable rotational speed is attributed to the conservative estimates for the UTS based on the hardness (*32*) and the assessment of failure based on Rankine's theory (*33*). Some plastic ductile material flow near the axis of rotation is likely to occur, redistributing and thereby lowering the stress inside the rotor. The highest measured rotational speed was slightly above 40 Mrpm and was reached with a spherical rotor of 0.5 mm in diameter.

The bursting of rotors was recorded by means of high-speed photography and is shown in Fig. 4. No obvious deformation of the rotor is visible before explosion. Slight optical distortions are due to the circular glass vacuum tube. After hitting the walls of the glass tube, the latter is destroyed by the inertia of the rotor fragments. The images confirm that the achievable rotational speed is only limited by the mechanical stress limit of the rotor and that the latter is stably levitated until material failure occurs.

Microscopic images of recovered rotor fragments show that most of the larger fragments exhibit a wedge shape (Fig. 5A) and no significant deformation of the outer spherical contour is observed. Some of the edges seem damaged and are contaminated by glass particles because of collision with the vacuum tube. Closer inspection of an exemplary surface of one of the fragments (Fig. 5B) exhibits characteristics typical of brittle tensile failure, which validates the appropriateness of the used failure criterion. Three-dimensional analysis of the same surface (Fig. 5C) shows that there are no apparent voids or defects at which stress concentration and commencement of the failure could have occurred, which is in agreement with the theory of Beams (*31*).

DISCUSSION

Here, rotational speeds slightly above 40 Mrpm were reached with a spherical rotor of 0.5 mm in diameter shortly before bursting, which is, to our knowledge, the highest measured rotational speed attained by an electrically driven rotor to date. At this rotational frequency, a circumferential

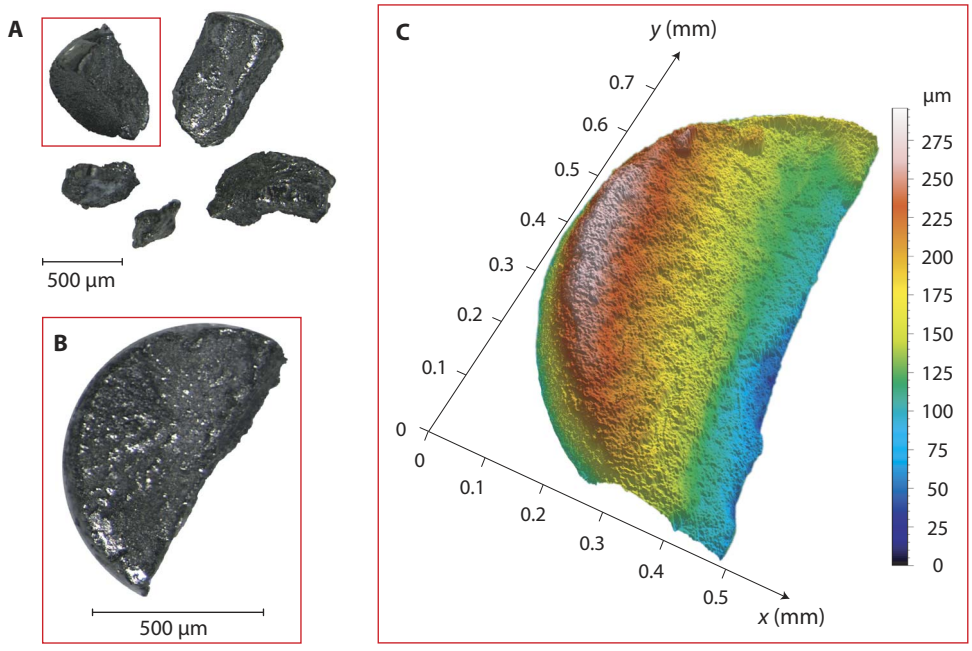

Fig. 5. Microscope images of exploded rotor fragments. (**A**) Overview of recovered larger wedge-shaped rotor fragments of a 0.8-mm-diameter rotor. (**B**) Detailed view of one exemplary surface of the fragments (red box) exhibiting typical properties of mostly brittle failure. (**C**) Three-dimensional view of the same surface highlighting its structure.

speed of 1047 m/s and a centrifugal acceleration of 4.4×10^8 g were reached. The realized motor setup allows the rapid and reproducible acceleration of ferromagnetic and conductive rotors with diameters of less than 1.5 mm. We have exemplarily demonstrated its use in the field of materials science for the study of tensile failure of millimeter-scale rotors. The conducted experiments allow the development of failure models, which are in good agreement with practical observations and could be extended to other small-scale particles. Aside from this example, the findings provide the means for further research into the general behavior of matter at ultrahigh centrifugal accelerations. They further enable the development of future micromagnetic bearings (*34*–*36*), small-scale motors, and high-speed electric drive systems, which we envision to be an essential part of a sustainable energy future.

MATERIALS AND METHODS

Sensors, actuators, and control of the magnetic suspension

The optical sensor system for measuring the rotor position, which is required as the input for its closed-loop control, consists of two near-infrared LEDs (LD 274, Osram) with wavelength $\lambda = 950$ nm and two two-dimensional PSDs (S5990-01, Hamamatsu). The PSDs generate photocurrents depending on the position of the rotor shadow on their active area. These currents are converted into voltages by operating amplifier circuits, which are sampled by analog-to-digital converters and relayed to a field programmable gate array (FPGA) (Cyclone III, Altera). The latter implements digital filters and proportional-integral-derivative controllers.

To achieve a high magnetic force per coil current, the electromagnet for vertical suspension of the rotor uses ferromagnetic hollow steel and centering cores and consists of ~350 windings of copper wire, resulting in an inductance of several hundreds of microhenries. To improve the dynamics of adjusting the coil current, an additional controller was used, forming a cascaded control structure (*37*) with the controller for the vertical position. The amplification factors for the proportional, integral, and derivative parts are tuned digitally to result in stabilization of the rotor without vertical oscillations.

The four coils used for driving the rotor and stabilizing it in horizontal direction consist of 11 turns each, which are wound around a core made from ferrite material to guide the magnetic flux. Litz wire was used to decrease the skin and proximity effects occurring at the high magnetic field frequencies used for driving the rotor. The inductance of these coils is in the range of a few microhenries, and the outputs of the position controllers were used directly to control the currents necessary for horizontal stabilization of the rotor. Two separate controllers with the same parameters were used for the x and y direction, respectively. To implement the necessary additional damping of rotor oscillations, generally, only the differential part of these controllers was used.

All coil currents for magnetic suspension of the rotor were generated using custom pulse-width modulated H-bridge switching converters as power amplifiers, which are controlled by the FPGA. The currents necessary for generating the rotating magnetic field to drive the rotor were provided using an adapted block commutation switching scheme (*38*). The control structure for stabilizing the rotor is visualized in fig. S2, and fig. S3 provides a comparative analysis of the horizontal rotor dynamics with and without active damping.

Rotational speed measurement and torque calculation

The rotational speed was measured by putting a black mark onto the rotor before an experiment. The layer of applied color is sufficiently thin and lightweight such that it does not result in any relevant imbalances. Upon rotation, the alternation between this mark and the remaining polished rotor surface yields modulation of the scattered light with a frequency corresponding to that of the rotation. The scattered light was observed via an optical fiber by a photo amplifier connected to an oscilloscope (MSO6034A, Agilent). The frequency of the modulated signal was determined by calculating its fast Fourier transform using the corresponding function implemented on the oscilloscope, which has a worst-case resolution of 500 Hz for the considered rotational frequencies.

Using $T = I\dot{\omega}_m \approx I\Delta\omega_m/\Delta t$ to obtain the torque acting on the rotor directly from measured data requires the calculation of the angular acceleration as the small difference of two comparably large quantities containing measurement noise. To avoid the problems associated with this procedure, a polynomial was fitted to the experimental data. Only data points with an error between this polynomial and the measured values of less than 0.5% (usually smaller) and at instants for which measurement values exist were used to obtain the angular acceleration.

Mechanical preparation and testing of samples

Rotors from the same production batch as those used in the acceleration experiments were prepared by grinding and polishing to expose different inner surfaces of the samples. On these surfaces, the Vickers hardness was determined at multiple locations using a microhardness tester (MXT-α, Wolpert). All measured values were within 5% of their mean for rotors without thermal treatment and within 2% for rotors, which had been thermally treated. The mean value of the measurements was used in the outlined calculations. Thermal treatment consisted of heating the rotors to 650°C with subsequent slow cooling to room temperature over several hours.

High-speed photography of explosions

A high-speed camera (FASTCAM SA1.1, Photron) was used to record the rotor explosions. The low exposure time requires high-intensity lighting, which was provided by a high-brightness LED (SL073, Advanced Illumination) pointed directly into the camera lens from the opposite side of the rotor. The resulting images show the rotor shadow. At 100,000 fps, the attainable image resolution is 192×160 pixels with a spatial resolution of ~23 μm per pixel for the chosen field of view.

Fragment analysis

Initial inspection of rotor fragments was carried out using a zoom microscope (M205 FA, Leica). The shown multifocus images were generated by recording a stack of multiple images focused on different parts of the fragments. Three-dimensional surface structures of the fragments were recorded using a laser scanning confocal microscope (LSM 880, Zeiss). The acquired data of the shown image (Fig. 5C) have a spatial resolution of 0.35 μm in the x and y directions and 0.49 μm in the z direction, respectively.

SUPPLEMENTARY MATERIALS

Supplementary material for this article is available at http://advances.sciencemag.org/cgi/content/full/4/1/e1701519/DC1

fig. S1. Photograph of the experimental setup with levitated rotor.

fig. S2. Control structure of the magnetic suspension system.

fig. S3. Rotor dynamics in horizontal direction with and without active magnetic damping.

REFERENCES AND NOTES

1. C. Zwyssig, J. W. Kolar, S. D. Round, Megaspeed drive systems: Pushing beyond 1 million r/min. *IEEE ASME Trans. Mechatron.* **14**, 564–574 (2009).

2. A. Borisavljevic, H. Polinder, J. A. Ferreira, On the speed limits of permanent-magnet machines. *IEEE Trans. Ind. Electron.* **57**, 220–227 (2010).
3. G. F. Marshall, G. E. Stutz, *Handbook of Optical and Laser Scanning* (CRC Press, 2011).
4. A. H. Epstein, Millimeter-scale, micro-electro-mechanical systems gas turbine engines. *J. Eng. Gas Turbines Power* **126**, 205–226 (2004).
5. F. T. Holmes, Axial magnetic suspensions. *Rev. Sci. Instrum.* **8**, 444–447 (1937).
6. J. W. Beams, Production and use of high centrifugal fields. *Science* **120**, 619–625 (1954).
7. R. Katano, S. Shimizu, Production of centrifugal fields greater than 100 million times gravity. *Rev. Sci. Instrum.* **50**, 805–810 (1979).
8. A. Boletis, H. Bleuler, Three axis AMB high speed micro motor, *Proceedings of the 9th International Symposium on Magnetic Bearings*, Lexington, KY, August 3–6, 2004 (Curran Associates Inc., 2007), pp. 544–549.
9. B. E. Kane, Levitated spinning graphene flakes in an electric quadrupole ion trap. *Phys. Rev. B* **82**, 115441 (2010).
10. Y. Arita, M. Mazilu, K. Dholakia, Laser-induced rotation and cooling of a trapped microgyroscope in vacuum. *Nat. Commun.* **4**, 2374 (2013).
11. A. Lehmuskero, R. Ogier, T. Gschneidtner, P. Johansson, M. Käll, Ultrafast spinning of gold nanoparticles in water using circularly polarized light. *Nano Lett.* **13**, 3129–3134 (2013).
12. K. Kim, X. Xu, J. Guo, D. L. Fan, Ultrahigh-speed rotating nanoelectromechanical system devices assembled from nanoscale building blocks. *Nat. Commun.* **5**, 3632 (2014).
13. A. L. Balk, L. O. Mair, P. P. Mathai, P. N. Patrone, W. Wang, S. Ahmed, T. E. Mallouk, J. A. Liddle, S. M. Stavis, Kilohertz rotation of nanorods propelled by ultrasound, traced by microvortex advection of nanoparticles. *ACS Nano* **8**, 8300–8309 (2014).
14. L. O. Mair, B. A. Evans, A. Nacev, P. Y. Stepanov, R. Hilaman, S. Chowdhury, S. Jafari, W. Wang, B. Shapiro, I. N. Weinberg, Magnetic microkayaks: Propulsion of microrods precessing near a surface by kilohertz frequency, rotating magnetic fields. *Nanoscale* **9**, 3375–3381 (2017).
15. L. Shao, Z.-J. Yang, D. Andrén, P. Johansson, M. Käll, Gold nanorod rotary motors driven by resonant light scattering. *ACS Nano* **9**, 12542–12551 (2015).
16. M. Schuck, T. Nussbaumer, J. W. Kolar, Characterization of electromagnetic rotor material properties and their impact on an ultra-high speed spinning ball motor. *IEEE Trans. Magn.* **52**, 8204404 (2016).
17. P. S. Epstein, On the resistance experienced by spheres in their motion through gases. *Phys. Rev.* **23**, 710–733 (1924).
18. Y. W. Yap, J. E. Sader, Sphere oscillating in a rarefied gas. *J. Fluid Mech.* **794**, 109–153 (2016).
19. J. W. Beams, Magnetic suspension for small rotors. *Rev. Sci. Instrum.* **21**, 182–184 (1950).
20. T. Reichert, T. Nussbaumer, J. W. Kolar, Complete analytical solution of electromagnetic field problem of high-speed spinning ball. *J. Appl. Phys.* **112**, 104901 (2012).
21. W. H. H. Banks, The laminar boundary layer on a rotating sphere. *Acta Mech.* **24**, 273–287 (1976).
22. D. H. Gabis, S. K. Loyalka, T. S. Storvick, Measurements of the tangential momentum accommodation coefficient in the transition flow regime with a spinning rotor gauge. *J. Vac. Sci. Technol. A* **14**, 2592–2598 (1996).
23. J. K. Fremerey, The spinning rotor gauge. *J. Vac. Sci. Technol. A* **3**, 1715–1720 (1985).
24. H. K. D. H. Bhadeshia, Steels for bearings. *Prog. Mater. Sci.* **57**, 268–435 (2012).
25. T. L. Bergman, F. P. Incropera, *Fundamentals of Heat and Mass Transfer* (John Wiley & Sons, 2011).
26. E. H. Kennard, *Kinetic Theory of Gases* (McGraw-Hill Book Co., 1938).
27. G. S. Springer, Heat transfer in rarefied gases. *Adv. Heat Transf.* **7**, 163–218 (1971).
28. A. I. Lurie, A. Belyaev, *Three-Dimensional Problems in the Theory of Elasticity* (Springer, 2005), pp. 243–407.
29. J. R. Davis, *Metals Handbook* (ASM International, 1998).
30. E. V. Zaretsky, Rolling bearing steels—A technical and historical perspective. *Mater. Sci. Technol.* **28**, 58–69 (2012).
31. J. W. Beams, Some experiments on the bursting of spherical rotors by centrifugal forces. *Proc. Soc. Exp. Stress Anal.* **7**, 1 (1949).
32. E. J. Pavlina, C. Van Tyne, Correlation of yield strength and tensile strength with hardness for steels. *J. Mater. Eng. Perform.* **17**, 888–893 (2008).
33. J. A. Collins, *Failure of Materials in Mechanical Design: Analysis, Prediction, Prevention* (John Wiley & Sons, 1993).
34. M. K. Ghantasala, L. Qin, D. K. Sood, R. B. Zmood, Design and fabrication of a micro magnetic bearing. *Smart Mater. Struct.* **9**, 235 (2000).
35. J. Kuroki, T. Shinshi, L. Li, A. Shimokohbe, A micro-magnetic bearing using capacitive axial displacement sensing. *Precis. Eng.* **30**, 54–62 (2006).
36. H. Bleuler, *Micro Magnetic Bearings* (Springer, 2009), pp. 487–503.
37. K. J. Aström, T. Hägglund, *Advanced PID Control* (Instrumentation, Systems and Automation Society, 2006).
38. M. H. Rashid, *Power Electronics Handbook: Devices, Circuits and Applications* (Academic Press, 2010).

Acknowledgments: We are grateful to J. Hugel for insightful discussions and his support of the project. We further acknowledge support of the Scientific Center for Optical and Electron Microscopy ScopeM of the Swiss Federal Institute of Technology (ETHZ). **Funding:** This work was supported by the ETH Zurich Foundation and the Else & Friedrich Hugel Fund for Mechatronics. **Author contributions:** J.W.K. and T.N. conceived and supervised the project. M.S. designed and performed the experiments, interpreted the results, and wrote the manuscript. D.S. contributed to interpreting the results and provided technical guidance. All authors discussed and approved the manuscript. **Competing interests:** The authors declare that they have no competing interests. **Data and materials availability:** All data needed to evaluate the conclusions in the paper are present in the paper and/or the Supplementary Materials. Additional data related to this paper may be requested from the authors.

Submitted 9 May 2017
Accepted 29 November 2017
Published 5 January 2018
10.1126/sciadv.1701519

Citation: M. Schuck, D. Steinert, T. Nussbaumer, J. W. Kolar, Ultrafast rotation of magnetically levitated macroscopic steel spheres. *Sci. Adv.* **4**, e1701519 (2018).

Ultrafast rotation of magnetically levitated macroscopic steel spheres

Marcel Schuck, Daniel Steinert, Thomas Nussbaumer and Johann W. Kolar

Sci Adv **4** (1), e1701519.
DOI: 10.1126/sciadv.1701519